On-shot laser beam diagnostics for high-power laser facility with phase modulation imaging

You may also be interested in:

Accurate focal spot diagnostics based on a single shot coherent modulation imaging
Xiaoliang He, S P Veetil, Cheng Liu et al.

Wavefront correction by target-phase-locking technology in a 500 TW laser facility
D E Wang, W J Dai, K N Zhou et al.

Measurement of thermal distortion in high power laser glass elements using ptychography
H Wang, Suhas P Veetil, C Liu et al.

Near-field ptychography using lateral and longitudinal shifts
A-L Robisch, K Kröger, A Rack et al.

Coherent x-ray diffraction imaging of paint pigment particles by scanning a phase plate modulator
Bo Chen, Fucai Zhang, Felisa Berenguer et al.

Application of optical diffraction method in designing phase plates
Ze-Min Lei, Xiao-Yan Sun, Feng-Nian Lv et al.

Formation of the uniform irradiation of a target in high-power laser facilities
Sergey G Garanin, Vladimir N Derkach and Roman A Shnyagin

Iterative reconstruction of thermally induced phasedistortion in a Nd3 + :YVO4 laser
Ludovic Grossard, Agnès Desfarges-Berthelemot, Bernard Colombeau et al.

Simultaneous optical image compression and encryption using error-reduction phase retrieval algorithm
Wei Liu, Zhengjun Liu and Shutian Liu

On-shot laser beam diagnostics for high-power laser facility with phase modulation imaging

X Pan[1], S P Veetil[2], C Liu[1], H Tao[1], Y Jiang[1], Q Lin[1], X Li[1] and J Zhu[1]

[1] Shanghai Institute of Optics and Fine Mechanics, Chinese Academy of Sciences, Shanghai 201800, People's Republic of China
[2] Department of Engineering Technology and Science, Higher Colleges of Technology, Fujairah 1626, United Arab Emirates

E-mail: cheng.liu@hotmail.co.uk

Abstract

A coherent-modulation-imaging-based (CMI) algorithm has been employed for on-shot laser beam diagnostics in high-power laser facilities, where high-intensity short-pulsed lasers from terawatt to petawatt are designed to realize inertial confinement fusion (ICF). A single-shot intensity measurement is sufficient for wave-front reconstruction, both for the near-field and far-field at the same time. The iterative reconstruction process is computationally very efficient and was completed in dozens of seconds by the additional use of a GPU device to speed it up. The compact measurement unit—including a CCD and a piece of pre-characterized phase plate—makes it convenient for focal-spot intensity prediction in the target chamber. It can be placed almost anywhere in high-power laser facilities to achieve near-field wave-front diagnostics. The feasibility of the method has been demonstrated by conducting a series of experiments with diagnostic beams and seed pulses with deactivated amplifiers in our high-power laser system.

Keywords: phase retrieval, laser beam characterization, diffractive optics, image reconstruction techniques

S Online supplementary data available from stacks.iop.org/LPL/13/055001/mmedia

(Some figures may appear in colour only in the online journal)

1. Introduction

The performance of a high-power laser facility (HPLF) heavily depends on the quality of the laser beam produced there [1, 2]. However, there are many factors leading to the deterioration of beam quality, such as material defects, thermal distortion, manufacturer error, gas density variations and the presence of dust in the environment. These factors would result in a non-ideal or deformed wave-front, which could cause serious problems such as self-focusing [3], leading to serious damage to optical components, decreased couple efficiency [4], and eventually, the degradation of the performance of the entire facility [5]. This highlights the importance of laser beam quality diagnostics and accurate focus prediction in the routine running of an HPLF. Apart from the most commonly used techniques based on the direct imaging of near-field and far-field wave-fronts, several methods [6] have been proposed to monitor the changes that occur in the phase distribution of the laser wave-front. Although interferometers [7] are reliable and highly accurate, their complex structure and the high demands they make on the environment make it practically difficult for them to take side-by-side measurements. The Shack–Hartmann sensor is one such commonly used device in the field of high-power lasers for monitoring

the phase of the laser beam with a compact structure. In fact, it has been successfully used for accurate focal-spot diagnostics at full energy in the OMEGA EP Laser System with careful calibration [8]. Nevertheless, the wave-front measured by the Shack–Hartmann sensor is a weighted average of the phase slopes taken across each micro-lens, and it is not very efficient for steep local wave-front slopes or large slope variations [9]. Furthermore, the finite number and size of the microlenses are additional obstacles to targeting higher resolution. As a consequence, the near-field approach in [8] has to face the challenges associated with the limitations of the Shack–Hartmann sensor. The ideal laser beam diagnostics device used in an HPLF should count on the convenience of the Hartmann sensor while providing a resolution level comparable to that of an interferometer. It is still a challenging task to achieve both things in side-by-side beam quality diagnostics in an HPLF. Phase retrieval, which has been proved to be an efficient technique for wave-front reconstruction in the field of visible light [10, 11], x-ray [12, 13] and electron imaging [14, 15] with one or several intensity measurements, could be an alternative tool to existing techniques for wave-front estimation in an HPLF considering its theoretically diffraction-limited resolution and simple setup [16, 17]. Several meaningful pieces of work based on phase retrieval for focal-spot characterization on the beam lines of the OMEGA EP have been done by Bahk *et al* [8, 18, 19]. A recent phase retrieval scheme works with one near-field measurement and several multiplane focal-spot intensity measurements, which is easy to accomplish in the target chamber [18]. A wave rms (root mean square) within 0.07 is available between phase retrieval and direct measurement in the test-bed setup. Fine agreement between phase retrieval and direct measurement is also observed in the multi-terawatt system when the glass amplifiers are not activated. A phase retrieval scheme based on the gradient-search algorithm has been employed to improve the poor focal-spot intensity prediction of the wave-front sensor [19] by retrieving the differential piston phase in the OMEGA EP beam. The mean cross-correlation between direct measurement and phase retrieval prediction has improved from 0.78 to 0.94 among a large number of on-shot measurements. The phase retrieval algorithm has been proved to be a reliable method for wave-front measurement and focal-spot prediction in an HPLF.

In this paper, a novel phase retrieval algorithm based on the phase modulation and coherent modulation imaging (CMI) proposed by Zhang [20–22] is demonstrated to provide an alternative scheme for wave-front diagnostics in an HPLF, and the basic experiments for focal-spot prediction have been reported by He [23]. Unlike previously used coherent diffractive imaging methods with multiple measurements which guarantee convergence, CMI uses only a single-shot diffraction intensity and is able to achieve a fast convergence speed due to random phase modulation. The compactness of the measurement unit, including a CCD (charge-coupled device) and a pre-characterized phase plate, makes it easy to place in the target chamber or anywhere in the HPLF. The feasibility of the developed device has been verified by a series of experiments in our high-power laser system for both the diagnostic beam and the seed pulse.
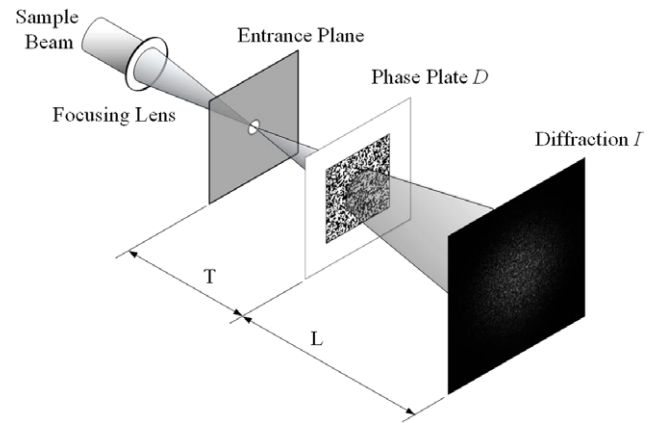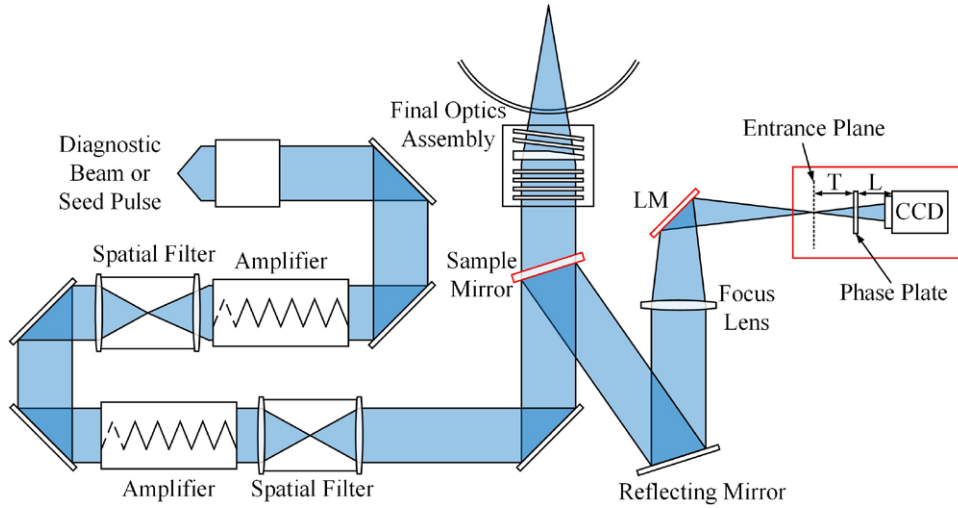

Figure 1. The basic scheme of beam diagnostics based on phase modulation.

2. Principle of wave-front reconstruction

The basic setup for wave-front reconstruction is illustrated in figure 1. Only the portion of the beam which needs to be diagnosed is shown in the figure. The sample beam is converged by a focusing lens. The entrance plane is chosen as the focal plane where the beam propagates through a small hole. A single-shot diffraction pattern, I, is recorded after the sample beam is scattered by a pre-characterized phase plate, D. If the setup is located in the target chamber, the beam which comes out of the final optic assembly in the HPLF is already converging; hence the focusing lens can be omitted from the setup. It should be noted that the small hole in the entrance plane, no matter whether real or virtual, is regarded as a rigid constriction during the iteration process and responsible for the success of phase reconstruction.

The reconstruction of the wave-front in the entrance plane is realized through iterations between three planes: the diffraction plane, phase plate plane and entrance plane. The distance between them is marked as T and L respectively. With numerical computation, it was also possible to retrieve the wave-front in any other plane—near or far-field—at the same time. If the setup is located in the target chamber, the intensity distribution in the entrance plane is exactly the same as the focal-spot prediction. For near-field wave-front diagnostics outside the chamber, it is necessary to subtract the phase of the focusing lens along with accurate calibration. The reconstruction process starts with a random guess, ϕ_1, of the incident wave in the entrance plane and is similar to the algorithm in [20] but with minor changes. The nth iteration is briefly described as follows:

(1) Propagate ϕ_n from the entrance plane to the phase plate plane at a distance T and obtain $\varphi_n = \mathfrak{I}[\phi_n, T]$, where $\mathfrak{I}$ represents the propagation operator.

(2) Multiply φ_n by the transmission function of phase plate D and propagate it further by a distance L to the diffraction plane. The corresponding estimation of diffraction is $\psi_n = \mathfrak{I}[\varphi_n D, L] = E_n \exp(\mathrm{i}\omega_n)$, where E_n and ω_n are the amplitude and phase respectively.

(3) Replace E_n with the $\sqrt{I}$ (square root of recorded diffraction intensity) while keeping the phase ω_n unchanged. The revised diffraction wave is $\psi_n' = \sqrt{I} \exp(\mathrm{i}\omega_n)$.

Figure 2. The basic scheme for single-shot beam diagnostics in high-power laser systems.

(4) Back propagate ψ'_n to the phase plate plane and update the incident wave as

$$\varphi'_n = \varphi_n + \frac{|D|}{|D_{max}|}\frac{D^*}{|D|^2+\alpha}\beta(\mathfrak{J}^{-1}[\psi'_n, L] - \varphi_n D) \quad (1)$$

where α and β are appropriately chosen constants and $\mathfrak{J}^{-1}$ represents the back propagation process.

(5) Propagate φ'_n back to the entrance plane and then obtain a new estimation of entrance wave according to equation (2).

$$\phi_{n+1} = S_{R(n)}\mathfrak{J}^{-1}[\varphi'_n, T] + \gamma(1 - S_{R(n)})(\mathfrak{J}^{-1}[\varphi'_n, T] - \phi_n). \quad (2)$$

The parameter γ is an appropriately chosen constant. $S_{R(n)}$ is a zero-padding logical mask with a value of 1 inside the central circle, while its radius $R(n)$ increases with the iteration number n and goes up until the maximum, R_{max}.

(6) Repeat steps 1–5 until the sum squared error RMS $= \sum|E_n^2 - I|^2 / \sum I^2$ is sufficiently small. The reconstructed wavefront in the entrance plane is the focal-spot prediction and the near-field wave-front can be numerically calculated after accurate calibrations.
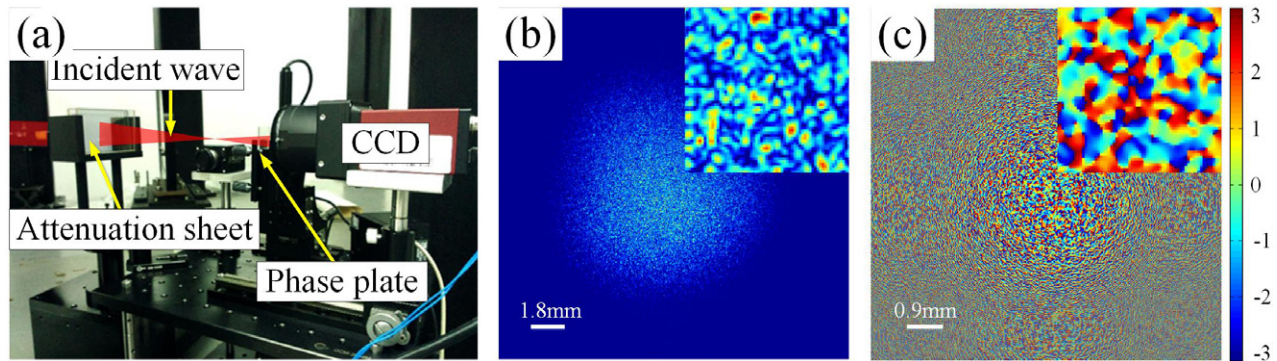
3. Experiment

A series of experiments have been completed in our high-power laser system, which is under construction at the Shanghai Institute of Optics and Fine Mechanics, CAS. Figure 2 shows the basic scheme of the system. The diagnostic setup, including the recording device (CCD) and pre-characterized phase plate, is shown in a box marked in red. The experiments were completed with a diagnostic beam and seed pulse (both at 1053 nm, 1 Hz) when the amplifiers are not activated. The diagnostic beam, which is on the order of microseconds, is used for collimation and assembly while the seed pulse, on the order of nanoseconds, is used for the routine running of the HPLF. Laser pulses with a diameter of 300 mm are introduced by the sample mirror located in front of the final optic

assembly and focused by a lens with a focal length of 2.75 m. The sample beam is then scattered by the phase plate located beyond the focal spot after reflection by the mirror LM. The recording device used in the experiments is a CCD with a cell size of 9 μm and the distance between focal spot, phase plate and recording device are $T = 80.3$ mm and $L = 72.3$ mm respectively. The binary phase delay, 0 or π, designed for a 1053 nm laser pulse with a dimension of 18 μm $\times$ 18 μm, is randomly allocated in a 20 mm $\times$ 20 mm section at the center of the phase plate. The phase plate is pre-characterized with the ePIE (extended ptychographical iterative engine) algorithm after mounting it on a motorized biaxial translation stage. In eliminating translation errors, positional error correction algorithms [24–26] were also employed for more accurate characterization. A quantity of 225 diffraction patterns with a matrix size of 2048 $\times$ 2048 pixels were recorded for reconstruction, despite the resulting computations being time consuming indeed. A GPU device, NVIDIA Tesla K40c, was used to speed up the computation by more than 20 times in comparison to an i7 CPU for the same computation load. It is worth mentioning that the actual reconstructed phase plate could be represented by $D = \gamma E(x,y)e^{i(\alpha x + \beta y)}$ where γ, α, and β are constants and $E(x,y)$ is the exact complex transmission function of the phase plate. Since there is no difference in the diffraction pattern when the probe beam is divided by the phase slope $\gamma e^{i(\alpha x + \beta y)}$, the factor $\gamma e^{i(\alpha x + \beta y)}$ does not interfere with accurate wave-front diagnostics or focal-spot intensity prediction.

Figures 3(a) and (b) illustrate the artificial phase plates and the microscopic images respectively. The phase delay differences come from the different etching depth on the quartz substrate. The parts of the reconstructed phase plate including amplitude and phase are shown in figures 3(c) and (d) respectively. As designed, the reconstructed phase delay between the sections of black and gray in figure 3(d) is about π for a 1053 nm laser pulse. Figure 3(e) shows the phase profile along the red dashed line in figure 3(d), and it is obvious that the phase delay difference is close to π, while a distinct phase slope exists along the horizontal coordinate. The phase
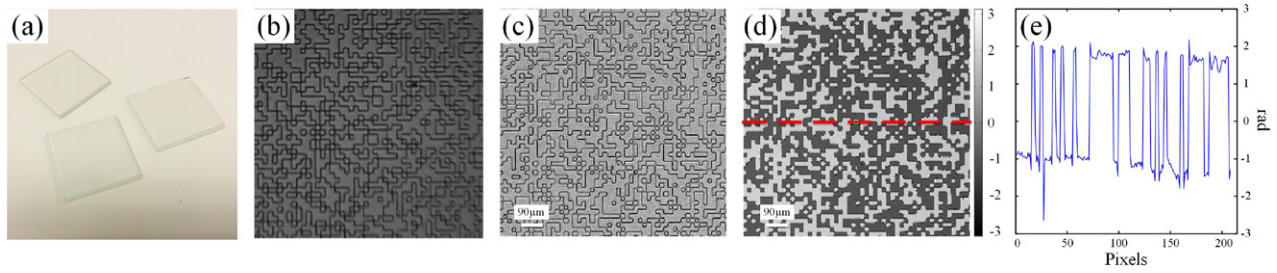
Figure 3. (a) Photo of the manufactured phase plate and (b) its microscopic image. (c) The reconstructed amplitude and (d) phase of the phase plate with the ePIE algorithm. The scale bar in (c) and (d) is 90 μm. The binary phase delay is random, 0 or π, designed for a 1053 nm laser pulse. The plot (e) is the phase profile taken across the red dashed line in (d) and the horizontal coordinate showing the pixel size and vertical coordinate is in radians.


Figure 4. (a) Experiment setup; (b) the recorded diffraction pattern and (c) the reconstructed phase of (b) (the corresponding iterative process is illustrated by media 1 (stacks.iop.org/LPL/13/055001/mmedia)). The scale bars in (b) and (c) are 1.8 mm and 0.9 mm respectively. The scale bar on the right of (c) is in radians.

saltation and noise in figures 3(c) and (d) are inevitable with the ePIE algorithm. Although the phase plate has a size of 20 mm $\times$ 20 mm, only a section of about 8 mm $\times$ 8 mm makes sense, due to the size of the incident wave on the phase plate. The black borderline throughout the phase plate in figures 3(b) and (c) comes from the absence of high-order information due to the finite numerical aperture (NA) of the microscope and the CCD, and hence reduces the phase plate characterization precision. Furthermore, the error will inevitably affect the final resolution of the wave reconstruction and should be reduced as much as possible.

After all the diffraction patterns have been recorded, the phase plate should be moved to center by the translation stage and the relative position between the phase plate and the CCD is also determined. Figure 4(a) shows the main part of the experiment setup, including the CCD, phase plate and attenuation sheet. The sample beam is also shown by the red drawing. The setup can be made more compact if the phase plate is mounted on the CCD after removing the translation stages when pre-characterization is finished. A sample of a recorded single-shot diffraction pattern is shown in figure 4(b), which was done after the calibration of the optical path. The magnified view in the top-right corner of figure 4(b) provides more details. The energy of the diffraction pattern is scattered over a wider section with homogenized intensity and leads to a more mutual interference between different orders of diffractions. This is helpful for taking full advantage of the CCD's dynamic range, and at the same time, also leads to a faster convergence of iterations. The reconstruction starts with a random guess of

the entrance wave in the focal plane and is completed in 27 s after 400 iterations with a matrix size of 2048 $\times$ 2048. The speed of the calculation can be further accelerated if C++ is used in place of Matlab. Figure 4(c) shows the corresponding reconstructed phase distribution of figure 4(b) with distinct details in the inset. The dynamic process of reconstruction for a diagnostic beam is illustrated by media 1.

Figures 5(a)–(f) show the reconstructions of the diagnostic beam and seed pulse respectively. The reconstructed amplitude and phase of the sample wave, φ, falling on the phase plate are illustrated in figures 5(a) and (b) respectively. The scale bar on them is 900 μm. The shape of the retrieved wave in figure 5(a) is a square with obvious straight-edge diffraction. This is because the size of the incident wave is larger than the reflecting mirror LM shown in figure 1. However, most of the energy in the incident wave is reflected successfully by the LM by a width of about 4.6 mm. The mirror LM is included to avoid propagation in a straight forward direction because of space constraints in the lab. As shown in figure 5(b), the illumination on the phase plate is similar to a spherical wave, while a relatively weak wave-front distortion is submerged in the phase, having a large gradient introduced by the focusing lens. The experiment was also repeated with the seed pulse and the retrieved amplitude and phase of the incident wave in the same plane are shown in figures 5(d) and (e) respectively. The phase distribution is similar to figure 5(b), but the amplitude is circular with a diameter of 3.2 mm. This is because there is an additional hole placed between the LM and the entrance plane for intense attenuation of the focal spot, as shown in the 3D
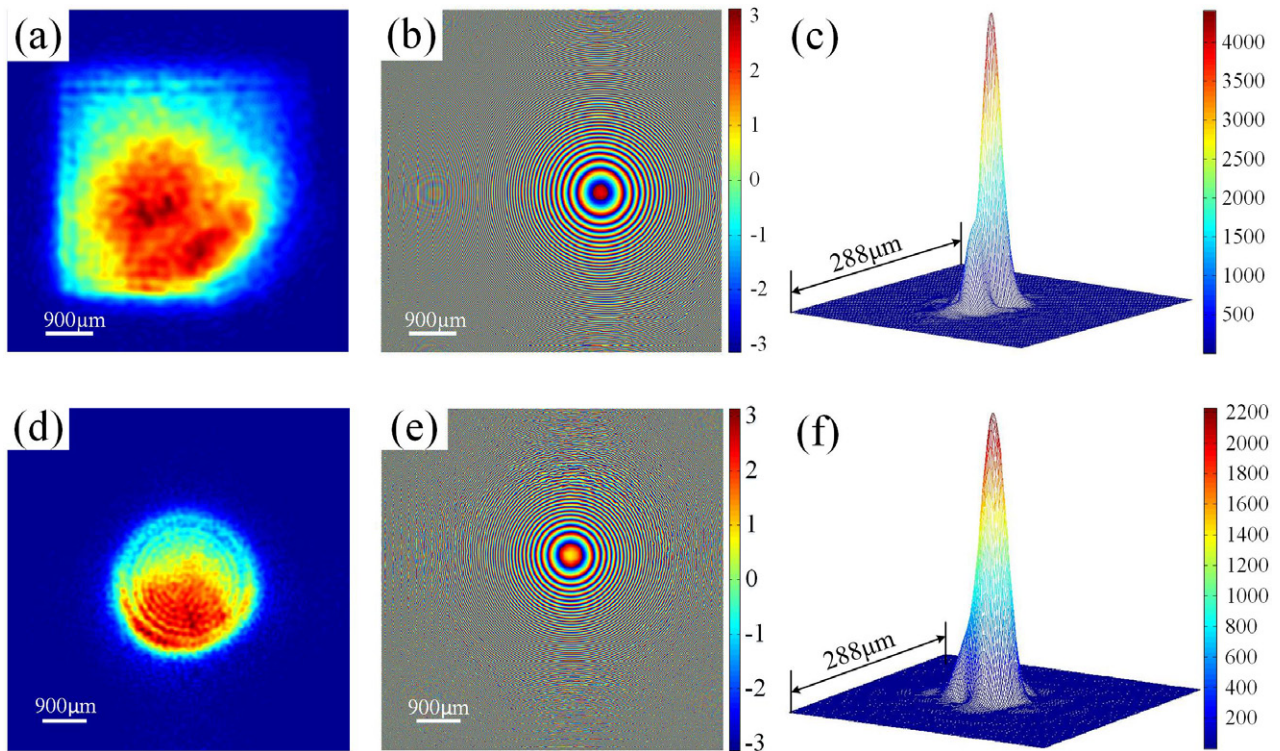
Figure 5. (a)–(f) are the results of the diagnostic beam and seed pulse respectively. The reconstructed amplitude and phase of the sample beam on the phase plate are illustrated in (a) and (b) respectively; (c) is the 3D intensity plot of the focal spot; (g) and (h) are the amplitude and phase of the wave closely in front of the phase plate respectively; (j) is the 3D focal-spot intensity of the seed pulse. The maximums in (c) and (f) are about 4300 and 2200 respectively. The unit of the colorized scale bar on the right of (b) and (c) is rad.

plot of the focal-spot intensity of the seed pulse in figure 5(f). Compared to the focal-spot intensity of the diagnostic beam in figure 5(c), the maximum intensity is only about 2200, while the corresponding value for the diagnostic beam is about 4300. Since the pre-characterized phase plate is $D = \gamma E(x,y)e^{i(\alpha x + \beta y)}$, according to energy conservation, the amplitude of the retrieved wave in front of the phase plate is to be multiplied by γ^{-1} compared to the actual value. In our experiments, the amplitude of the complex transmittance of the phase plate $\gamma E(x,y)$ obtained by ePIE ranges around 30, while it should be less than 1 for a quartz substrate. As a consequence, the actual dynamic range of focal-spot intensity should be much bigger than 2200 when considering the factor γ, which is a fatal obstacle for the direct measurement of far-field intensity with a CCD of finite dynamic range—especially in the target chamber.

The encircled energy of the far-field wave is one of the most important parameters for high-power laser facilities. For example, the defense-related goal for the National Ignition Facility is that 50% of all designated energy—1.8 MJ for 192 beams— should be converged within 100 μm in a 600 μm Hohlraum target. Figure 6(a) illustrates the revolution of encircled energy within the circles of a different radius on the focal spot of the diagnostic beam and seed pulse. The red and blue lines represent the seed pulse and diagnostic beam respectively. The variation trends for both of them are similar and the corresponding encircled energy R_{80} and R_{90} is about 30.6 μm and 45 μm respectively. This is about 2.6 times and 3.8 times the diffraction-limited focal-spot energy size for R_{80} and R_{90} respectively, ignoring the lost energy due to the

mirror LM. The hole located between the LM and the entrance plane for the seed pulse may account for the lower encircled energy for the same radius compared to the diagnostic beam. Since the energy concentration can be calculated, the relative positions of the focal spot can also be measured to evaluate the stability of laser beams in high-power laser facilities. Figure 6(b) illustrates the statistical focal-spot positions of 255 consecutive shots in 255 s, and the blue dots represent the position of the highest energy points of the seed pulse focal spot. It can be seen that the focal spots randomly jitter within a circle of 41.4 μm in diameter. This instability mainly comes from air distortion due to air-conditioning and people walking around, rather than thermal distortion and gas density variations, considering that the amplifiers are not activated.

Unlike other direct diagnostic techniques, a notable advantage of phase retrieval is that it can also be extended to retrieve the wave-front at any arbitrary plane by numerical computation. This is illustrated in figure 7, where a series of diagnostic beam intensities were generated at several planes spaced out evenly on either side of the focal plane. This is a simple yet efficient way to analyze beam distribution in any arbitrary plane with accurate calibration. Characterizing the complex transmission function in the focal plane precisely would mean that the complex transmission function in the near-field was also available simultaneously. Figure 8 provides another example of near-field wave-front diagnostics taken just in front of the focusing lens by assuming that the lens is ideal without any aberrations. The reconstructed amplitude is shown in figure 8(a). The phase part is shown in figure 8(b)
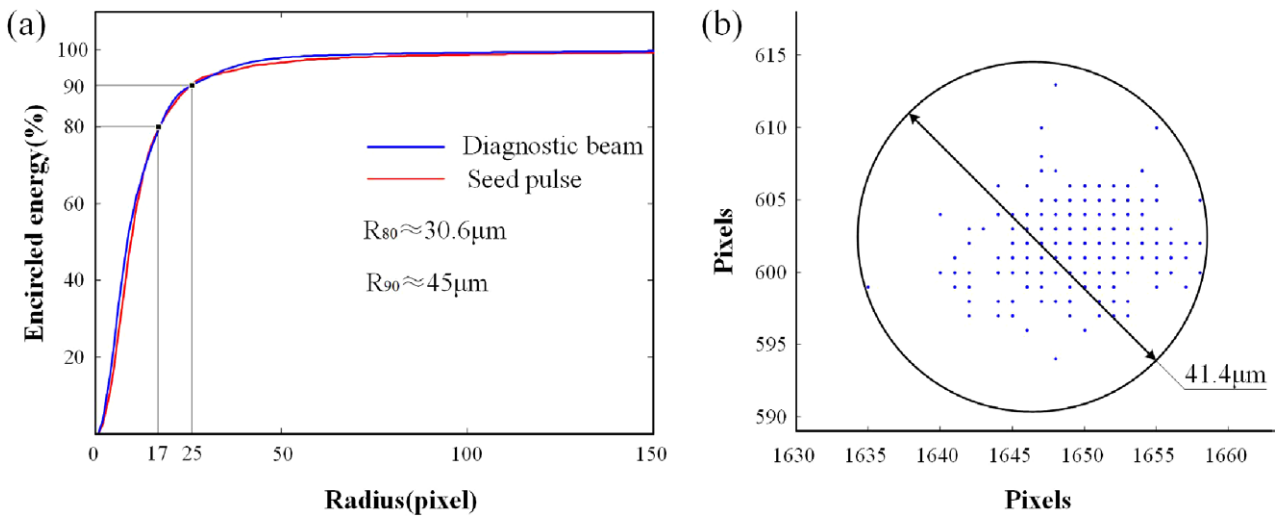
Figure 6. (a) Shows the encircled energy for the diagnostic beam and seed pulse; the length of each pixel is 1.8 μm; (b) is the retrieved focal-spot distribution for 255 seed pulses with consecutive single-shots in 255 s. The focal spots jitter in the circle with a diameter of 41.4 μm.
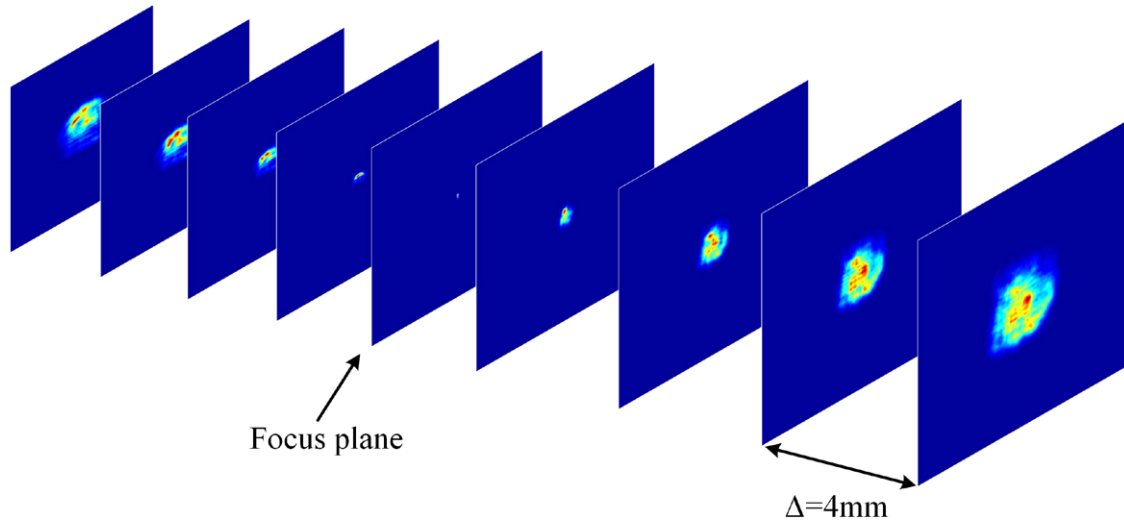

Figure 7. The intensity in a series of planes with a different deviation distance to focus plane according to numerical calculations. The distance between the adjacent planes is 4 mm.
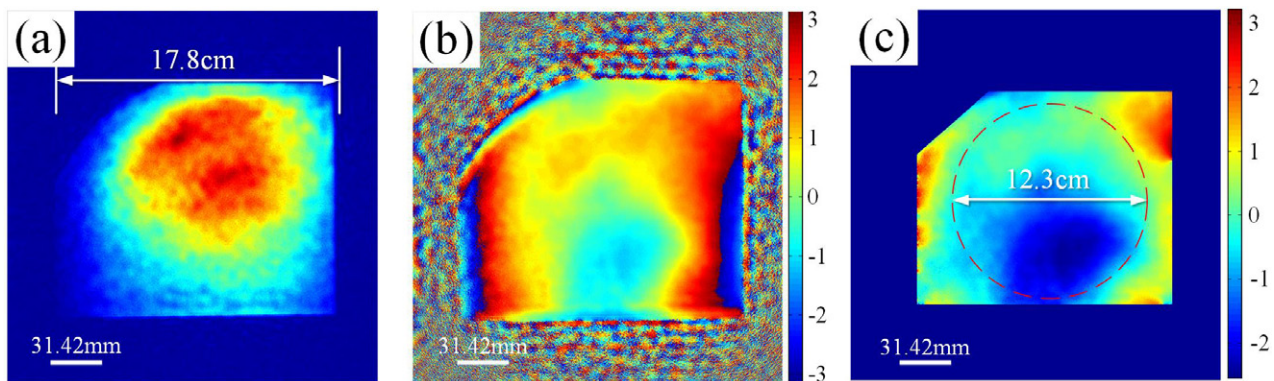
Figure 8. (a) The amplitude of the diagnostic beam just before the convergent lens with a width of 17.8 cm. (b) The corresponding phase distribution of the sample beam; (c) the unwrapped phase of (b) where the peak-to-valley value in the central circle with a diameter of 12.3 cm is 3.26 rad. The vertical scales are in radians.

with the corresponding unwrapped phase in figure 8(c). The figures show only a part of the diagnostic beam, as it was not fully reflected by the mirror LM with a dimension less than the beam width. Aberrations in the lens must be taken into account to obtain a very accurate description of the wave-front in such cases.
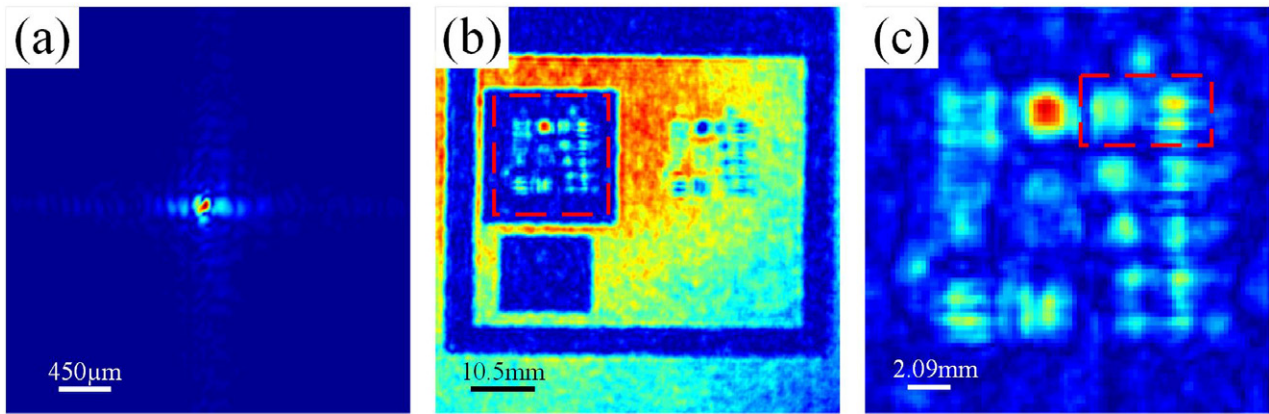
Figure 9. (a) and (b) are the amplitude reconstructed in the focal plane and lens plane respectively, after placing a standard test target (USAF 1951) close to the focusing lens. (c) A magnified view of the details marked inside the red dashed line in (b). Separation between the two recognizable lines in (c) is about 1.05 mm.

The spatial resolution of the setup is studied using a test target with a dimension of 63 mm × 63 mm. Figure 9(a) shows the reconstructed intensity distribution at the entrance plane with obvious diffraction fringes. Figure 9(b) shows the reconstructed images at the focusing lens plane. A magnified portion of the reconstructed test target is shown in figure 9(c). The completely distinguishable line pair is group 0, line 2 (marked by red dashed lines in figure 9(c)) with 1.12 lines pairs per mm. There should actually be three lines in that line group, however only two lines are distinguishable from each other. The distance between the two recognizable lines is about 1.05 mm. The resolution is lower in this case as, due to the undersized mirror LM, the higher order information was lost. However, besides the LM, there are several other intrinsic factors which limit the achievable resolution of the final reconstruction. The first one is the performance of the recording device, which determines the accuracy of the recorded diffraction pattern. Although the phase plate, regarded as a strong scattering object, reduces the dynamic range demands on the recording device, the high-order diffraction pattern with weak intensity is always easily affected by noise and abandoned due to the limited NA of the device. Another factor which limits the resolution comes from the characterization precision of the phase plate. The strong scattering ability of the phase plate with random binary phase delay, 0 or π, makes it more difficult to reconstruct with the ePIE algorithm. Pre-characterization precision obviously relies on the capability of ePIE, although positional errors have been corrected by other algorithms. The phase retrieval precision for the CMI cannot surpass ePIE in principle if the pre-characterization process does not employ other algorithms. This means that the CMI technique partially sacrifices its precision for faster convergence with the single-shot diffraction pattern compared to ePIE. Moreover, there is no doubt that the smaller unit size of the phase plate means faster convergence, but also causes more difficulty for the pre-characterization process with high accuracy. Rigid precision evaluation and its improvement will be taken up in subsequent works.

4. Conclusion

Accurate near-field wave-front diagnostics and focal-spot prediction are the basic diagnostic requirements of high-power laser facilities. While wave-front diagnostics based on the Shack–Hartmann sensor face certain inherent limitations, a method based on phase retrieval appears to be more reliable, promising to give more flexibility and better results. In this paper, a novel phase retrieval algorithm based on phase modulation is employed for wave-front diagnostics, and its validity is demonstrated by a series of experiments on a diagnostic beam and seed pulse in our high-power laser system without activating the amplifiers. Its compact structure, including a CCD and pre-characterized phase plate, leads to a more flexible configuration no matter whether it is placed in the target chamber or any other part of the HPLF. Furthermore, only a single-shot diffraction pattern is sufficient for wave-front reconstruction in any arbitrary plane by numerical calculations. These extensive applications could be employed in high-power laser facilities both for far-field prediction and near-field diagnostics after the necessary calibrations.

Acknowledgments

References

[1] Zacharias R A *et al* 2004 Alignment and wavefront control systems of the National Ignition Facility *Opt. Eng.* **43** 2873–84
[2] Wang H, Liu C, He X, Pan X, Zhou S, Wu R and Zhu J 2014 Wavefront measurement techniques used in high-power lasers *High Power Laser Sci. Eng.* **2** e25
[3] Marburger J 1975 Self-focusing: theory *Prog. Quantum Electron.* **4** 35–110
[4] Wegner P J *et al* 2004 NIF final optics system: frequency conversion and beam conditioning *Proc. SPIE* **5341** 180

[5] Kato Y *et al* 1984 Random phasing of high-power lasers for uniform target acceleration and plasma-instability suppression *Phys. Rev. Lett.* **53** 1057–60

[6] Koch J A *et al* 2000 Experimental comparison of a Shack–Hartmann sensor and a phase-shifting interferometer for large-optics metrology applications *Appl. Opt.* **39** 4540–6

[7] Latychevskaia T, Longchamp J-N and Fink H-W 2012 When holography meets coherent diffraction imaging *Opt. Express* **20** 28871–92

[8] Bromage J *et al* 2008 A focal-spot diagnostic for on-shot characterization of high-energy petawatt lasers *Opt. Express* **16** 16561–72

[9] Groening S, Sick B, Donner K, Pfund J, Lindlein N and Schwider J 2000 Wave-front reconstruction with a Shack–Hartmann sensor with an iterative spline fitting method *Appl. Opt.* **39** 561–7

[10] Rodenburg J M, Hurst A C and Cullis A G 2007 Transmission microscopy without lenses for objects of unlimited size *Ultramicroscopy* **107** 227–31

[11] Pan X, Liu C and Zhu J 2013 Single shot ptychographical iterative engine based on multi-beam illumination *Appl. Phys. Lett.* **103** 171105

[12] Enders B, Dierolf M, Cloetens P, Stockmar M, Pfeiffer F and Thibault P 2014 Ptychography with broad-bandwidth radiation *Appl. Phys. Lett.* **104** 171104

[13] Peterson I *et al* 2012 Nanoscale Fresnel coherent diffraction imaging tomography using ptychography *Opt. Express* **20** 24678–85

[14] Humphry M J, Kraus B, Hurst A C, Maiden A M and Rodenburg J M 2012 Ptychographic electron microscopy using high-angle dark-field scattering for sub-nanometre resolution imaging *Nat. Commun.* **3** 730

[15] Hüe F, Rodenburg J M, Maiden A M, Sweeney F and Midgley P A 2010 Wave-front phase retrieval in transmission electron microscopy via ptychography *Phys. Rev.* B **82** 121415

[16] Rodenburg J M 1989 The phase problem, microdiffraction and wavelength-limited resolution—a discussion *Ultramicroscopy* **27** 413–22

[17] Rodenburg J M 2008 Ptychography and related diffractive imaging methods *Advances in Imaging and Electron Physics* vol 150, ed P W Hawkes (Toulouse: Elsevier) pp 87–184

[18] Bahk S-W, Bromage J, Begishev I A, Mileham C, Stoeckl C, Storm M and Zuegel J D 2008 On-shot focal-spot characterization technique using phase retrieval *Appl. Opt.* **47** 4589–97

[19] Kruschwitz B E, Bahk S W, Bromage J, Moore M D and Irwin D 2012 Accurate target-plane focal-spot characterization in high-energy laser systems using phase retrieval *Opt. Express* **20** 20874–83

[20] Zhang F and Rodenburg J M 2010 Phase retrieval based on wave-front relay and modulation *Phys. Rev.* B **82** 121104

[21] Tao H, Veetil S P, Cheng J, Pan X, Wang H, Liu C and Zhu J 2015 Measurement of the complex transmittance of large optical elements with modulation coherent imaging *Appl. Opt.* **54** 1776–81

[22] Zhang F, Pedrini G and Osten W 2007 Phase retrieval of arbitrary complex-valued fields through aperture-plane modulation *Phys. Rev.* A **75** 043805

[23] Xiaoliang H, Veetil S P, Cheng L, Shumei G, Yueke W, Jicheng W and Zhu J 2015 Accurate focal spot diagnostics based on a single shot coherent modulation imaging *Laser Phys. Lett.* **12** 015005

[24] Beckers M, Senkbeil T, Gorniak T, Giewekemeyer K, Salditt T and Rosenhahn A 2013 Drift correction in ptychographic diffractive imaging *Ultramicroscopy* **126** 44–7

[25] Maiden A M, Humphry M J, Sarahan M C, Kraus B and Rodenburg J M 2012 An annealing algorithm to correct positioning errors in ptychography *Ultramicroscopy* **120** 64–72

[26] Zhang F *et al* 2013 Translation position determination in ptychographic coherent diffraction imaging *Opt. Express* **21** 13592–606